Matter and Radiation at Extremes REVIEW scitation.org/journal/mre

Non-resonant inelastic X-ray scattering spectroscopy: A momentum probe to detect the electronic structures of atoms and molecules

Cite as: Matter Radiat. Extremes 5, 054201 (2020); doi: 10.1063/5.0011416
Submitted: 21 April 2020 • Accepted: 13 July 2020 •
Published Online: 31 July 2020

Shu-Xing Wang[1,2] and Lin-Fan Zhu[1,2,a)]

AFFILIATIONS

[1]Hefei National Laboratory for Physical Sciences at the Microscale and Department of Modern Physics, University of Science and Technology of China, Hefei, Anhui 230026, China
[2]Synergetic Innovation Center of Quantum Information and Quantum Physics, University of Science and Technology of China, Hefei, Anhui 230026, China

Note: This paper is part of the Special Issue on Atomic and Molecular Physics for Controlled Fusion and Astrophysics.
[a)]**Author to whom correspondence should be addressed:** lfzhu@ustc.edu.cn

ABSTRACT

Non-resonant inelastic X-ray scattering (NRIXS) is a new technique for atomic and molecular physics that allows one to measure the electronic structures and dynamic parameters of the ground and excited states of atoms and molecules in momentum space. There is a clearly understood physical picture of NRIXS, which reveals its remarkable advantages of satisfying the first Born approximation and being able to excite dipole-forbidden transitions. Various physical properties of atoms and molecules, such as their elastic and inelastic squared form factors, optical oscillator strengths, and Compton profiles, can be explored using NRIXS under different experimental conditions. In this paper, we review newly developed experimental methods for NRIXS, together with its characteristics and various applications, with emphasis on the new insights into excitation mechanism and other new information revealed by this technique. The intrinsic connections and differences between NRIXS and fast electron impact spectroscopy are elucidated. Future applications of this method to atomic and molecular physics are also described.

I. INTRODUCTION

Atomic and molecular dynamic parameters are closely related to electronic structure, i.e., to the wave functions of ground and excited states. The experimental acquisition of benchmark dynamic parameters with high accuracy and high resolution can deepen our understanding of atomic and molecular structure, as well as providing a stringent test of theoretical methods and computational models. In general, there are three main experimental techniques to approach electronic structures on an absolute scale for neutral atoms and molecules: the photoabsorption method, fast electron impact, and inelastic X-ray scattering. As its name suggests, the photoabsorption method is used to determine photoabsorption cross sections, which are equivalent to optical oscillator strengths (OOSs) at near-zero momentum transfer. Fast electron impact and inelastic X-ray scattering have the merit of determining the electronic structures of the ground and excited states of atoms and molecules in momentum space, including the case of zero momentum transfer. Furthermore, a cross-check among the experimental results obtained by different methods can exclude possible systematic experimental errors and provide benchmark atomic and molecular data for use in simulation models and for testing theoretical methods. These tested theoretical methods and computational codes can then be used to construct reliable atomic and molecular databases, which have wide applications across a number of disciplines, including plasma physics, fusion physics and engineering, astrophysics, condensed matter physics, materials science, chemistry, biology, and atmospheric sciences. In this review, we summarize recent developments in non-resonant inelastic X-ray scattering, and we limit our scope to applications in atomic and molecular physics.

X-rays provide a powerful probe to explore the structure and dynamics of atoms and molecules, which promises not only to help solve problems in applied physics, but also to test our understanding of quantum electrodynamics, relativity, and many-body phenomena.[1] The first X-ray scattering experiment dates back to 1923, when

Compton and Debye offered an explanation of inelastic X-ray scattering, which revealed the particle-like nature of photons experimentally.[2,3] The pioneering inelastic X-ray scattering experiment carried out by DuMond[4] on solid beryllium confirmed the validity of Fermi–Pauli statistics for the distribution of electron velocities in metals, and his subsequent experimental studies opened the door to the investigation of the electronic structure of matter. Because of the extremely low scattering cross sections involved (about 8×10^{-26} cm^2), these experiments were very difficult to perform owing to the limited brilliance and energy resolution of the X-ray beams as well as the data acquisition efficiency available at that time. The advent of rotating-anode X-ray tubes and scintillation counters in the mid-1960s improved the X-ray flux and the detection efficiency greatly and facilitated the exploration of X-ray scattering in diverse areas of condensed matter physics. Experimental tools such as Compton scattering, magnetic Compton scattering, non-resonant X-ray scattering, and X-ray Raman scattering were developed. Physical quantities such as the Compton profile, dynamic structure factors, and spin densities could thus be determined. The renaissance of X-ray scattering techniques can be attributed to the availability of high-brilliance and tunable synchrotron radiation photon sources, especially those at third-generation synchrotron radiation facilities. Since the 1970s, the energy resolution and efficiency of X-ray scattering have improved dramatically. Nowadays, the brilliance of the X-rays from synchrotron radiation is more than 12 orders of magnitude higher than that of early X-ray tubes. In addition, advanced crystal analyzers and high-resolution detectors offer opportunities for fine structure studies. X-ray scattering spectrometers with low, moderate, and high energy resolutions of about 1 eV, 70 meV, and as small as 0.1 meV have been installed at synchrotron radiation facilities all around the world. Free-electron lasers (FELs) with much higher brilliance, such as FLASH at DESY in Germany,[5] LCLS at SLAC in the USA,[6] and SACLA at RIKEN in Japan,[7] have been commissioned since 2010, and are now available for users. Furthermore, the fourth-generation synchrotron radiation sources, i.e., so-called diffraction-limit rings, such as the Beijing High Energy Photon Source, are under construction, and these will improve the brilliance to 10^{22} photons s^{-1} mm^{-2} mrad^{-2} (0.1% BW)$^{-1}$. All of these new photon sources provide opportunities for photon-hungry techniques, including X-ray scattering.

In X-ray scattering processes, the incident photon can transfer energy and momentum to the target. From the energy transfer, or so-called energy loss, the final energy state of the target can be identified. The momentum transfer can be applied to explore the electronic structure of the target in momentum space. By combining the energy loss and momentum transfer, the electronic structure of a definite state can be determined.[8,9] Furthermore, X-ray scattering has a unique advantage of exciting electric dipole-forbidden transitions. Therefore, it can be used to study such transitions, for example, electric monopolar, electric quadrupolar, and electric octupolar transitions at large momentum transfer, which are absent in photoabsorption spectra owing to the negligible momentum transfer and the restrictions imposed by selection rules.[8–11]

According to whether or not the electronic state of the target changes during the scattering process, X-ray scattering can be classified as inelastic (IXS) or elastic (EXS). The former includes inelastic excitation of the discrete valence- and inner-shell states (i.e., so-called Compton excitation) and Compton scattering in which the energy loss is beyond the ionization threshold and the excited electron is ejected into a continuous state. In addition, according to whether or not the incident photon energy matches an inner-shell excitation, IXS can be classified as resonant (RIXS) or non-resonant (NRIXS), with RIXS having a much larger cross section than NRIXS. For RIXS, high-order scattering amplitudes dominate cross sections, while NRIXS gives a simple physical picture in which the first-order scattering amplitude generally dominates the scattering and can be used directly to detect the electronic structure of the target.[3,8,9] As an experimental technique, NRIXS is traditionally applied in condensed matter physics, where the availability of high-density targets can partially circumvent the problems caused by the very low cross sections. For atomic and molecular physics, dilute gaseous targets of very low density, about three orders of magnitude lower than that of condensed matter, are commonly used, which makes experimental application of NRIXS extremely difficult. Therefore, high-resolution NRIXS was not utilized in atomic and molecular physics until the advent of third-generation synchrotron radiation sources. In this review, we focus on high-resolution NRIXS and its application to gaseous atoms and molecules.

The first experiment on X-ray scattering by gaseous CO_2 and Ar was performed in 1927,[12] although the results were brought into question by those of a subsequent experiment.[13] However, these pioneering works measured the angular distribution of the relative total X-ray scattering cross sections without energy resolution, due to the poor experimental conditions available then. The first energy-resolved X-ray scattering spectrum of gaseous atomic helium was recorded by DuMond and Kirkpatrick with an exposure of 2059 h, and the Compton profile of helium was obtained.[14] It is understandable that the experimental energy resolution and the signal-to-noise ratio were limited at that time. Subsequent advances in the study of the Compton profiles of atoms have only been achieved since the 1970s, using X-rays produced by rotating-anode X-ray tubes[15] and radiation sources,[16] with typical energy resolutions of several hundreds of eV. Owing to the limited energy resolution and low count rate, there was no investigation of discrete valence-shell excitations of atoms and molecules until 2010, when the first high-resolution NRIXS experiment on valence-shell excitations of helium was reported.[8] The high brilliance of the third-generation synchrotron radiation sources paves the way for high-resolution NRIXS experiments on gaseous atoms and molecules,[8,9] and NRIXS has now been used to reveal diverse physical properties of atoms and molecules, such as electronic structure in momentum space for both ground and excited states,[8,9,17–20] optical oscillator strengths (OOSs),[21] Compton profiles,[22–24] and integral cross sections (ICSs)[25–28] over a wide electron impact energy range. During these investigations, new experimental techniques such as the dipole (γ, γ) method have been proposed to determine OOSs,[21] and strict experimental protocols have been established. In addition, investigations combining NRIXS with other experimental techniques such as electron energy loss spectroscopy (EELS) has been performed.[8,9,21,25] Joint studies of the dynamic parameters of atoms and molecules with completely different experimental techniques offer an independent cross check and eliminate possible systematic experimental errors.[25,26] The extensive investigations carried out to date indicate that the dynamic parameters determined by NRIXS can serve as benchmark data for use in

plasma modeling, astrophysics, atmospheric physics, and other applications where they are needed. The measurements obtained can also offer a stringent test of relativistic and many-body effects, as well as of state-of-the-art theoretical models and computational codes that can produce these parameters.

In this review, we summarize NRIXS studies of atomic and molecular dynamic parameters, most of which were carried out by our group at the beamline BL12XU of SPring-8 over the past 10 years. In Sec. II, we present the theoretical foundations of the use of NRIXS to determine the atomic and molecular dynamic parameters. Experimental access to the dynamic parameters by means of NRIXS is presented in Sec. III, and, in particular, the absolutization method is described in detail. In Sec. IV, we list some typical experimental results obtained in recent years. Finally, in Sec. V, we summarize the achievements and give a general outlook of future plans for work with NRIXS.

II. THEORETICAL FOUNDATIONS

As shown schematically in Fig. 1, a photon with energy $\hbar\omega_i$, wave vector $\boldsymbol{k}_i$, and polarization ϵ_i is scattered by a target M from initial state i to final state f, and the scattered photon with energy $\hbar\omega_f$, wave vector $\boldsymbol{k}_f$, and polarization ϵ_f can be expressed as

$$\hbar\omega_i(\boldsymbol{k}_i, \epsilon_i) + M \rightarrow \hbar\omega_f(\boldsymbol{k}_f, \epsilon_f) + M^*. \tag{1}$$

Here, the thermal motion and recoil momentum of atomic and molecular targets can be neglected. The energy and momentum transfers to the target in the scattering process can be simplified as

$$\hbar\omega = \hbar\omega_i - \hbar\omega_f = E_f - E_i, \tag{2}$$

$$\boldsymbol{q} = \hbar\boldsymbol{k}_i - \hbar\boldsymbol{k}_f = \boldsymbol{q}_i - \boldsymbol{q}_f, \tag{3}$$

where E_i and E_f are the energies of the atom or molecule before and after scattering. The squared momentum transfer can be expressed as

$$q^2 = q_i^2 + q_f^2 - 2q_iq_f\cos 2\theta, \tag{4}$$

where 2θ is the scattering angle following the definition traditionally used in X-ray scattering.

According to the generalized Kramers–Heisenberg formula,[29] the double differential cross section (DDCS) associated with a transition of the scattering electron system from an initial state $|i\rangle$ to a final state $|f\rangle$ in X-ray scattering has the form

$$\frac{d^2\sigma}{d\Omega\, d\hbar\omega_f} = \left(\frac{e^2}{m_ec^2}\right)^2\left(\frac{\omega_f}{\omega_i}\right)|F_1 + F_2 + F_3 + F_4|^2\delta(E_i - E_f + \hbar\omega), \tag{5}$$

with the expressions:

$$F_1 = \langle f|\sum_j \exp(i\boldsymbol{q}\cdot\boldsymbol{r}_j)|i\rangle(\epsilon_i\cdot\epsilon_f^*), \tag{6}$$

$$F_2 = -i\left[\frac{\hbar(\omega_i+\omega_f)}{2m_ec^2}\right]\langle f|\sum_j \exp(i\boldsymbol{q}\cdot\boldsymbol{r}_j)(\sigma_j/2)|i\rangle\cdot(\epsilon_f^*\times\epsilon_i), \tag{7}$$

$$F_3 = \frac{\hbar^2}{m_e}\sum_n\sum_{jj'}\frac{\langle f|[\epsilon_f^*\cdot\boldsymbol{p}_j/\hbar - i(\boldsymbol{k}_f\times\epsilon_f)\cdot\sigma_j/2]\exp(-i\boldsymbol{k}_f\cdot\boldsymbol{r}_j)|n\rangle}{E_i - E_n + \hbar\omega_i - i\Gamma_n/2} \times\langle n|[\epsilon_i\cdot\boldsymbol{p}_{j'}/\hbar + i(\boldsymbol{k}_i\times\epsilon_i)\cdot\sigma_{j'}/2]\exp(i\boldsymbol{k}_i\cdot\boldsymbol{r}_{j'})|i\rangle, \tag{8}$$

$$F_4 = \frac{\langle f|[\epsilon_i\cdot\boldsymbol{p}_j/\hbar + i(\boldsymbol{k}_i\times\epsilon_i)\cdot\sigma_j/2]\exp(i\boldsymbol{k}_i\cdot\boldsymbol{r}_j)|n\rangle}{E_i - E_n - \hbar\omega_f} \times\langle n|[\epsilon_f^*\cdot\boldsymbol{p}_{j'}/\hbar - i(\boldsymbol{k}_f\times\epsilon_f)\cdot\sigma_{j'}/2]\exp(-i\boldsymbol{k}_f\cdot\boldsymbol{r}_{j'})|i\rangle, \tag{9}$$

where $\boldsymbol{r}_j$, $\boldsymbol{p}_j$, and $\boldsymbol{\sigma}_j$ are the position operator, momentum operator, and spin operator of the jth electron. When the incident photon energy falls into the direct vicinity of an inner-shell excitation energy, the spin-independent part of F_3, which is the scattering amplitude of RIXS, dominates the scattering amplitude. The non-resonant X-ray scattering amplitude is dominated by the charge-scattering term F_1. F_2, F_3 and F_4 are related to spin and orbital magnetic scattering, with negligible magnitude at an incident photon energy of 10 keV.[3] In a typical NRIXS experiment, the incident photon energy is set at about 10 keV, so it can easily be estimated that the contribution of the second term is less than 2% of that of the first term. The third term can be safely neglected since the incident photon energy is too high to satisfy the resonance condition. The fourth term is about four orders of magnitude lower than the first. Although there do exist interference terms that contribute to the measured DDCS, their contribution can safely be neglected since it is less than 2%, as analyzed above. Therefore, the following expression can be used to describe the DDCS for NRIXS:[3,9]

$$\frac{d^2\sigma}{d\Omega\, d\hbar\omega_f} = r_0^2\frac{\omega_f}{\omega_i}|\epsilon_i\cdot\epsilon_f^*|^2\sum_f|\langle f|\sum_j\exp(i\boldsymbol{q}\cdot\boldsymbol{r}_j)|i\rangle|^2 \times\delta(E_i - E_f + \hbar\omega), \tag{10}$$

where $r_0 \equiv e^2/m_ec^2$ is the classical electron radius. The definition of the Thomson differential cross section is introduced as

$$\left(\frac{d\sigma}{d\Omega}\right)_{\mathrm{Th}} \equiv r_0^2\frac{\omega_f}{\omega_i}|\epsilon_i\cdot\epsilon_f^*|^2. \tag{11}$$

The factor $|\epsilon_i\cdot\epsilon_f^*|^2$ equals $\cos^2 2\theta$ for completely linear polarized photons with polarization direction in the horizontal scattering plane, and equals 1 if the polarization direction of the scattered photon is perpendicular to the scattering plane. The residual part is defined as a

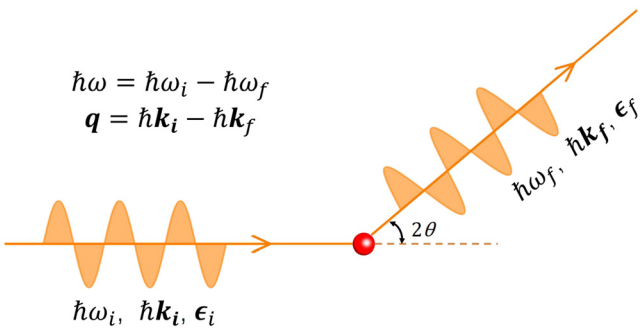

FIG. 1. Schematic of NRIXS.

dynamic structure factor in condensed matter physics, which describes the excitation strength of the scattering system from the initial state $|i\rangle$ to the final state $|f\rangle$:

$$S(\boldsymbol{q},\omega) = |\langle f|\sum_j \exp(i\boldsymbol{q}\cdot\boldsymbol{r}_j)|i\rangle|^2 \delta(E_i - E_f + \hbar\omega). \quad (12)$$

However, in contrast to the continuum IXS spectrum observed in condensed matter physics, the valence-shell or inner-shell excitations of atoms and molecules are discrete transitions. Therefore, the DDCS in Eq. (10) should be integrated over $\hbar\omega_f$ for a definite transition to obtain the differential cross section (DCS):

$$\left(\frac{d\sigma}{d\Omega}\right)_\gamma = \left(\frac{d\sigma}{d\Omega}\right)_{\mathrm{Th}} \zeta(\boldsymbol{q}), \quad (13)$$

where $\zeta(\boldsymbol{q})$ is the squared form factor (SFF), which can be determined experimentally by measuring the DCS for the X-ray scattering process:

$$\zeta(\boldsymbol{q}) = |\langle f|\sum_j \exp(i\boldsymbol{q}\cdot\boldsymbol{r}_j)|i\rangle|^2 = \frac{1}{r_0^2}\frac{\omega_i}{\omega_f}\frac{1}{|\epsilon_i\cdot\epsilon_f^*|^2}\left(\frac{d\sigma}{d\Omega}\right)_\gamma. \quad (14)$$

For inelastic scattering, $\zeta(\boldsymbol{q})$ is called the inelastic squared form factor (ISFF), which contains information about the wave functions of the excited states in momentum space. NRIXS has a merit that the first Born approximation (FBA) is always satisfied.[3,30] It is well known that there is a close connection between NRIXS and the EELS.[8,9] The quantities measured by these two techniques are interconvertible if the FBA is satisfied, which corresponds to high-energy electron impact. Since the FBA for electron scattering can be determined only by a trial-and-error procedure, the ISFF obtained by NRIXS can serve as the high-energy limit of electron impact and can be used to study the validity of the FBA in electron impact experiments.[20] Furthermore, joint study of the ISFF with both fast electron impact and NRIXS can give a cross check and produce benchmark ISFF data for cross-disciplinary studies, as well as providing deep insight into the scattering process. The cross-checked data can thus serve as a benchmark for stringent tests of the state-of-the-art theoretical codes.

When the energy loss of the incident photon is larger than the ionization threshold, the well-known Compton scattering process occurs:

$$\hbar\omega_i(\boldsymbol{k}_i,\epsilon_i) + M_i \rightarrow \hbar\omega_f(\boldsymbol{k}_f,\epsilon_f) + M_f^+ + e^-. \quad (15)$$

The momentum transfer of the Compton scattering can be considered under the framework of impulse approximation. As a result, the electron momentum distribution of the electron in the target will broaden the Compton scattering peak to give what is known as the Compton profile. Within the impulse approximation and taking the outgoing electron as a plane wave, the DDCS of the incident X-ray by the target can be described as[15,16]

$$\frac{d^2\sigma}{d\Omega\, d\hbar\omega_f} = \left(\frac{d\sigma}{d\Omega}\right)_{\mathrm{Th}}\frac{m_e}{\hbar q}\int n(\boldsymbol{p})\,dp_x\,dp_y = \left(\frac{d\sigma}{d\Omega}\right)_{\mathrm{Th}}\frac{m_e}{\hbar q}J(p_z), \quad (16)$$

where the z axis is along the $\boldsymbol{q}$ direction and $n(\boldsymbol{p}) = \sum_j|\psi_j(\boldsymbol{p})|^2$ is the probability of the electron with a momentum $\boldsymbol{p}$. Considering the energy conservation in the scattering process, p_z can be determined as

$$p_z = \frac{\omega m_e}{q} - \frac{\hbar q}{2}. \quad (17)$$

Here, $q = |\boldsymbol{q}_i - \boldsymbol{q}_f|$ and $\omega = \omega_i - \omega_f$ can be easily determined from the experimental scattering angle and the scattering photon energy. $J(p_z)$ is the well-known Compton profile:

$$J(p_z) = \sum_j \int_{p_x}\int_{p_y} \psi_j^*(\boldsymbol{p})\psi_j(\boldsymbol{p})\,dp_x\,dp_y, \quad (18)$$

It should be noted that the integral of the Compton profile over p_z is the number of target electrons. In principle, the Compton profile gives the electron momentum density of the target atom or molecule on the p_z axis. The experimentally measured Compton profile can be used to study the ground state wave function of a target.

If the energy transfer during the X-ray scattering process is zero, i.e., there is elastic scattering, then the final electronic state is same as the initial state. The elastic squared form factor (ESFF), which reflects the electronic structure of the ground state, can then be described as

$$\zeta(\boldsymbol{q}) = |\langle i|\sum_j \exp(i\boldsymbol{q}\cdot\boldsymbol{r}_j)|i\rangle|^2 = \frac{1}{r_0^2}\frac{\omega_i}{\omega_f}\frac{1}{|\epsilon_i\cdot\epsilon_f^*|^2}\left(\frac{d\sigma}{d\Omega}\right)_\gamma. \quad (19)$$

The ISFF can be used to determine different dynamic parameters under the corresponding approximations with different experimental arrangements. When we choose a small scattering angle 2θ under which the squared momentum transfer $q^2 \approx 0$, ISFF can be simplified by expanding the transition matrix element:

$$\begin{aligned}\zeta(\boldsymbol{q}) &= |\langle f|\sum_j \exp(i\boldsymbol{q}\cdot\boldsymbol{r}_j)|i\rangle|^2 \\ &= |\langle f|\sum_j\left[1 + \boldsymbol{q}\cdot\boldsymbol{r}_j + \frac{(\boldsymbol{q}\cdot\boldsymbol{r}_j)^2}{2!} + \frac{(\boldsymbol{q}\cdot\boldsymbol{r}_j)^3}{3!} + \cdots\right]|i\rangle|^2. \end{aligned} \quad (20)$$

The first term is zero because of the orthogonality of the wave functions between the initial and final states for inelastic scattering. The terms with high orders of $\boldsymbol{q}\cdot\boldsymbol{r}_j$ can be neglected because $q^2 \approx 0$. By choosing the direction of $\boldsymbol{q}$ as the z axis, the simplified transition matrix element can be expressed as

$$\lim_{q\rightarrow 0}|\langle f|\sum_j \exp(i\boldsymbol{q}\cdot\boldsymbol{r}_j)|i\rangle| = \lim_{q\rightarrow 0}|\langle f|\sum_j \exp(iqz_j)|i\rangle| = qM_n, \quad (21)$$

where

$$M_n = |\langle f|\sum_j z_j|i\rangle| \quad (22)$$

is the dipole matrix element. Thus, we can simulate the photoabsorption process at a small scattering angle with NRIXS, which is called the dipole (γ, γ) method.[21] The optical oscillator strengths $f_0(\omega_n)$ can be related to the DCS as follows:

$$f_0(\omega_n) = \frac{2\omega_n}{q^2}\zeta(\boldsymbol{q}) = \frac{2\omega_n}{q^2}\frac{1}{r_0^2}\frac{\omega_i}{\omega_f}\frac{1}{|\epsilon_i\cdot\epsilon_f^*|^2}\left(\frac{d\sigma}{d\Omega}\right)_\gamma. \quad (23)$$

III. EXPERIMENTAL METHODS

The low density of gaseous samples and their low X-ray scattering cross sections result in low counting rates. Therefore,

high-brilliance third-generation synchrotron radiation sources, such as SPring-8 and the Advanced Photon Source (APS), are a prerequisite for NRIXS experiments on gaseous atoms and molecules.[8,31] Furthermore, to utilize the limited and costly synchrotron radiation beam time efficiently, a special gas cell with two windows sealed by Kapton foil for photons in and photons out has been designed to support a high gas pressure up to 10 atm to improve the target density. A schematic view of a NRIXS spectrometer at the BL12XU beamline of SPring-8 is shown in Fig. 2(a). The incident photon flux is monitored by the ionization chamber in front of the gas cell. The scattered photons are collected by the analyzer, and those with a specific energy are reflected by the analyzer to the detector through a gas chamber filled with helium to reduce scattering loss in the air. In actual operation, the analyzer energy for the scattered photon is fixed at about 9890 eV while the incident photon energy varies, from which the energy loss can be deduced and the IXS spectrum recorded. A Si(333) monochromator and a diced Si(555) spherical crystal analyzer can achieve a high energy resolution of 70 meV.[8] The energy resolution can be improved to 25 meV when a Si(800) four-bounce channel-cut monochromator and a position-sensitive Si strip detector are used.[32]

The experimental DCS of NRIXS is determined through[33]

$$\frac{d\sigma(\omega_n, 2\theta)}{d\Omega} = \frac{N(\omega_n, 2\theta)}{N_0}\,\frac{1}{D_0\alpha}\,\frac{1}{l_{\text{eff}}}\,\frac{1}{n_0 P}, \tag{24}$$

where $N(\omega_n, 2\theta)$ and N_0 are the counts of the excitation peaks and the incident photon flux, with n denoting the specific transition studied. D_0 is a factor determined by the efficiencies of the ionization chamber and X-ray detector. Usually, a scanning spectrum covers an energy range of several eV, which is quite narrow compared with the incident photon energy of about 10 keV. Thus, D_0 can be regarded as constant. α is the transmittivity of the X-rays and is determined by the gas sample, gas pressure, and the Kapton foil. The ratio of the X-ray intensities passing through the gas cell with and without a sample in it is measured for this value. l_{eff} is the effective scattering length, as shown in Fig. 2(b). n_0 and P are the density of the target at 1 atm and the pressure of the target in units of atm.

At large scattering angles where the effective scattering length is less than the diameter of the gas cell in the scattering plane, l_{eff} can be expressed as[8]

$$l_{\text{eff}} = \frac{l_0}{\sin 2\theta}, \tag{25}$$

where l_0 is the scattering length at 90°. The ISFF can be determined from the following expression:

$$\begin{aligned}\zeta(\boldsymbol{q}) &= \frac{1}{r_0^2}\,\frac{\omega_i}{\omega_f}\,\frac{1}{|\epsilon_i\cdot\epsilon_f^*|^2}\left(\frac{d\sigma}{d\Omega}\right)_\gamma \\ &= \frac{1}{r_0^2}\,\frac{\omega_i}{\omega_f}\,\frac{1}{|\epsilon_i\cdot\epsilon_f^*|^2}\,\frac{N(\omega_n, 2\theta)}{N_0}\,\frac{1}{D_0\alpha}\,\frac{\sin 2\theta}{l_0}\,\frac{1}{n_0 P} \\ &= C\,\frac{\omega_i}{\omega_f}\,\frac{\sin 2\theta}{|\epsilon_i\cdot\epsilon_f^*|^2}\,\frac{N(\omega_n, 2\theta)}{N_0}\,\frac{1}{\alpha}\,\frac{1}{P}.\end{aligned} \tag{26}$$

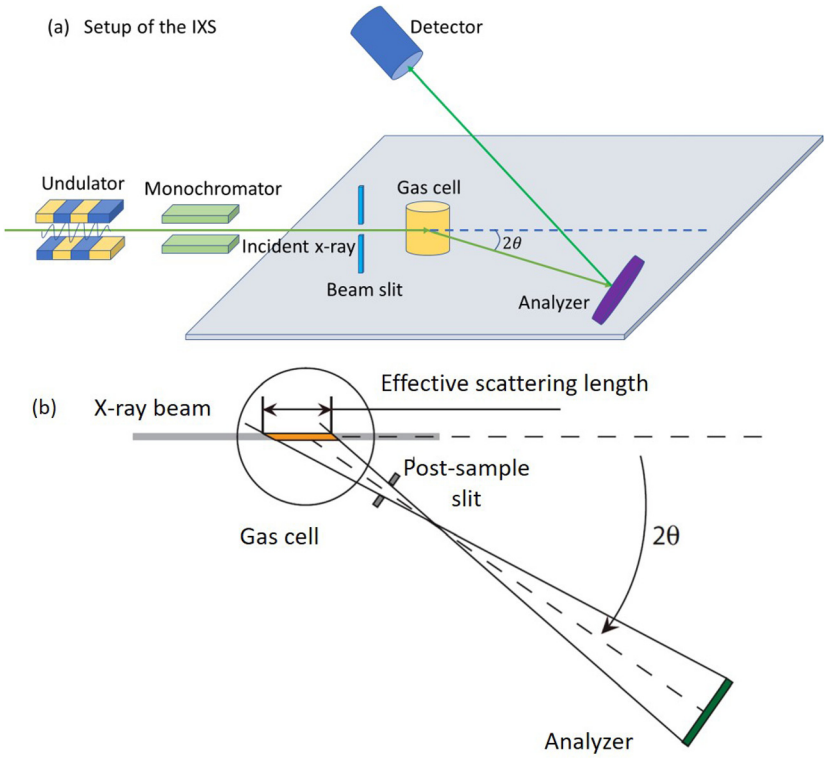

FIG. 2. Schematics of (a) the NRIXS experimental setup and (b) the effective scattering length.

All the parameters in Eq. (26) can be measured directly, and only the constant C is left to be determined:

$$C = \frac{1}{r_0^2 D_0 l_0 n_0}. \tag{27}$$

Fortunately, the ISFF from the ground state to the 2^1P state of the simplest monoatomic gas helium has been studied with high precision and accuracy both theoretically and experimentally.[8,9,34,35] Therefore, the ISFF of the 2^1P state of helium can serve as a calibration standard. When the DCS of the 2^1P state is measured under the same experimental conditions as those of the sample, the constant C can be determined simply as

$$C = \zeta(\boldsymbol{q})_{\mathrm{He}} \left(\frac{\omega_f}{\omega_i}\right)_{\mathrm{He}} \frac{|\epsilon_i \cdot \epsilon_f^*|^2}{\sin 2\theta} \left[\frac{N_0}{N(2\,^1P, 2\theta)}\right]_{\mathrm{He}} \alpha_{\mathrm{He}} P_{\mathrm{He}}, \tag{28}$$

where $\zeta(\boldsymbol{q})_{\mathrm{He}}$ is the benchmark ISFF of the 2^1P state of helium.[34,35] The absolute ISFFs for gaseous samples at large scattering angles can then be obtained with the aid of the determined C.

However, at small scattering angles where the effective scattering length will exceed the size of the gas cell, there is no analytical expression for l_{eff}. Therefore, the DCS for the 2^1P state of helium at the same scattering angle has to be measured for normalizing $\zeta(\boldsymbol{q})$ of the sample:

$$\zeta(\boldsymbol{q}) = \zeta(\boldsymbol{q})_{\mathrm{He}} \frac{\omega_i/\omega_f}{(\omega_i/\omega_f)_{\mathrm{He}}} \frac{N(\omega_n, 2\theta)/N_0}{(N(2\,^1P, 2\theta)/N_0)_{\mathrm{He}}} \frac{P_{\mathrm{He}}}{P} \frac{\alpha_{\mathrm{He}}}{\alpha}. \tag{29}$$

For the ESFF of the ground state when elastic scattering occurs, the experimental measurement and the normalization procedure are the same as for ISFF.

Another normalization method is the Bethe f-sum rule:[36]

$$N = \frac{2}{q^2} \int_0^\infty \omega S(q, \omega)\, d\omega, \tag{30}$$

where N is the number of electrons in the target. This absolutization method is often used in experiments at a low energy resolution of 1 eV, in which a wide energy loss region can be scanned.[31,37] However, one should be cautious, since Eq. (30) needs a fixed q but q increases with energy loss according to Eq. (4), and, in particular, a wide energy loss region should be measured for this method. Furthermore, the variations of D_0 and α in Eq. (24) should also be evaluated when $\hbar\omega_i$ covers a wider range.

In the dipole (γ, γ) method, the so-called Bethe–Born factor $B_\gamma(\omega_n)$ is introduced to connect the DCS with the OOS $f_0(\omega_n)$ at negligible momentum transfer as follows:[21]

$$f_0(\omega_n) = B_\gamma(\omega_n) \left(\frac{d\sigma}{d\Omega}\right)_\gamma, \tag{31}$$

where

$$B_\gamma(\omega_n) = \frac{2\omega_n}{q^2} \frac{1}{r_0^2} \frac{\omega_i}{\omega_f} \frac{1}{|\epsilon_i \cdot \epsilon_f^*|^2} = \frac{1}{r_0^2} \frac{2\omega_n\omega_i}{\omega_f} \frac{1}{q^2 \cos^2 2\theta}. \tag{32}$$

Here, the direction of linear polarization of the incident photon is in the scattering plane. Owing to the finite solid angle of the analyzer, the angular resolution function of the spectrometer is entangled with the measured DCS. Taking into account the angular resolution function, the so-called Bethe–Born conversion factor $B_\gamma'(\omega_n)$ is defined as

$$B_\gamma'(\omega_n) = \int B_\gamma(\omega_n) A(2\theta)\, d(2\theta) = \frac{1}{r_0^2} \frac{2\omega_n\omega_i}{\omega_f} \int \frac{1}{q^2 \cos^2 2\theta} A(2\theta)\, d(2\theta), \tag{33}$$

where $A(2\theta)$ is the angular resolution function of the spectrometer, which can be determined by simulating the actual arrangement of the light path taking account of the rectilinear propagation of light. The relative OOS is then written as

$$f_0^r(\omega_n) = B_\gamma'(\omega_n) \frac{N(\omega_n)}{N_0} \frac{1}{D_0\alpha} \frac{1}{l_{\mathrm{eff}}} \frac{1}{n_0 P}. \tag{34}$$

The OOS of the 2^1P state of He is chosen to normalize the measured OOS of the sample,[38] and the procedure is similar to that for the absolutization of the ISFF:

$$f_0(\omega_n) = \frac{B_{\gamma_n}'(\omega)}{B_\gamma'(2\,^1P)_{\mathrm{He}}} \frac{N(\omega_n)/N_0}{[N(2\,^1P)/N_0]_{\mathrm{He}}} \frac{\alpha_{\mathrm{He}}}{\alpha} \frac{P_{\mathrm{He}}}{P} f_0(2\,^1P)_{\mathrm{He}}. \tag{35}$$

The Compton profile is extracted from the Compton scattering spectrum, which is generally measured with a high photon energy at a large scattering angle. A schematic of the Compton scattering spectrometer on the BL1501 beamline of the Shanghai Synchrotron Radiation Facility (SSRF) is shown in Fig. 3.[22] The incident photon has a high energy of 20 keV with an energy spread of 3 eV, and a silicon drift X-ray detector is used to detect the scattered photons with an energy resolution of about 250 eV with a linear photon energy dependence. The higher incident photon energy and a larger scattering angle will help to improve the momentum resolution. Under the experimental conditions mentioned above, a momentum resolution of 1.5 a.u. is achieved.

The Compton profile is directly connected with the determined DDCS:[22]

$$J(p_z) = \frac{\hbar q}{m_e} \frac{1}{r_0^2} \frac{\omega_i}{\omega_f} \frac{1}{|\epsilon_i \cdot \epsilon_f^*|^2} \frac{d^2\sigma}{d\Omega\, d\hbar\omega_f} = C \frac{q}{\omega_f} N(\omega), \tag{36}$$

where C is a constant and $N(\omega)$ is the measured Compton scattering spectrum. The momentum along the z axis, p_z, can be easily obtained from the measured spectrum according to Eq. (17). The experimental

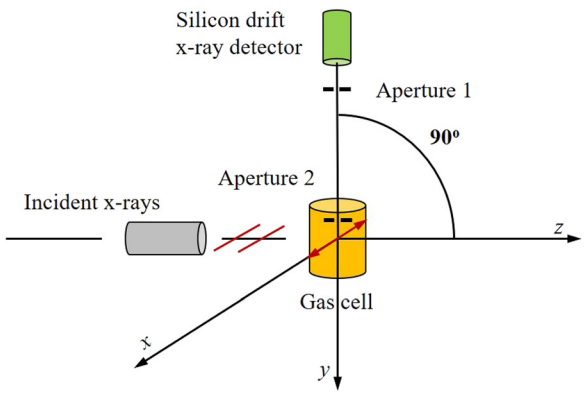

FIG. 3. Schematic of the Compton scattering spectrometer.

result can be absolutized to the atomic number Z by integrating it over p_z as mentioned above.

It is worth mentioning that the experimental uncertainties in the atomic and molecular dynamic parameters determined by NRIXS are mainly due to the statistical counts and the fitting procedure. The transmittivity and the pressures of both the target and helium, as well as the reference standard generalized oscillator strength (GOS) or OOS of the 2^1P state of helium, contribute an error of about 1%. The total uncertainties are strongly related to specific excitations. For well-resolved transitions, the statistical error dominates the uncertainty at the level of a few percent. In principle, it can be reduced by accumulating the counts, while it is hard to obtain a long beamtime. For heavily overlapped transitions, the uncertainties from the fitting procedure dominate the error bars. Generally speaking, the total experimental uncertainty is less than 10% for most transitions. The uncertainty can be as small as 3% for resolved strong transitions, but it can reach 30% for weak or overlapped transitions.

IV. TYPICAL RESULTS

By employing the NRIXS method, the ISFFs, ESFFs, OOSs, and Compton profiles for many gaseous atoms and molecules have been explored. Here, we will introduce various aspects of the applications of IXS, with emphasis on new insights into excitation mechanisms. IXS will be compared with EELS due to their intrinsic connection. The importance of cross-checking the experimental results determined by IXS and EELS to obtain benchmark dynamic parameters of the valence-shell excitations of gaseous atoms and molecules will be pointed out.

A. Inelastic squared form factor

At the first attempt, the state-resolved ISFFs for both the $1s^{21}\,S_0 \rightarrow 1s2s\,{}^1S_0$ electric monopolar transition and the $1s^{21}\,S_0 \rightarrow 1s2p\,{}^1P_1$ electric dipolar transition of atomic helium are used to demonstrate the validity of the NRIXS method.[8,9] Traditionally, the electronic structures of the ground state and excited states of gaseous samples are studied by high-energy EELS, for which it is believed the FBA is satisfied. Under the FBA, the electronic structures of atoms and molecules are generally represented by the generalized oscillator strengths (GOSs) in the EELS with the form[9]

$$\begin{aligned} f(q,E_n) &= \frac{E_n}{2}\frac{p_0}{p_a}q^2\left(\frac{d\sigma}{d\Omega}\right)_e \\ &= \frac{2E_n}{q^2}|\langle f|\sum_j \exp(i\boldsymbol{q}\cdot\boldsymbol{r}_j)|i\rangle|^2 \\ &= \frac{2E_n}{q^2}\zeta(q,\omega_n), \end{aligned} \tag{37}$$

where E_n is the corresponding excitation energy, and p_0 and p_a are the magnitudes of the initial and final electron momenta. It is clear that both NRIXS and EELS can be used to determine the ISFF when the FBA is satisfied by EELS.

Figure 4 presents selected NRIXS and EELS spectra at similar momentum transfers measured by our group.[8,9,39] Qualitatively, at the same squared momentum transfers, the IXS and EELS spectra in Fig. 4 are identical, i.e., the same features and the same relative intensities are observed. It should be stressed that completely different experimental techniques are used to obtain the spectra shown in Fig. 4, i.e., the probes, impact energies, and experimental conditions

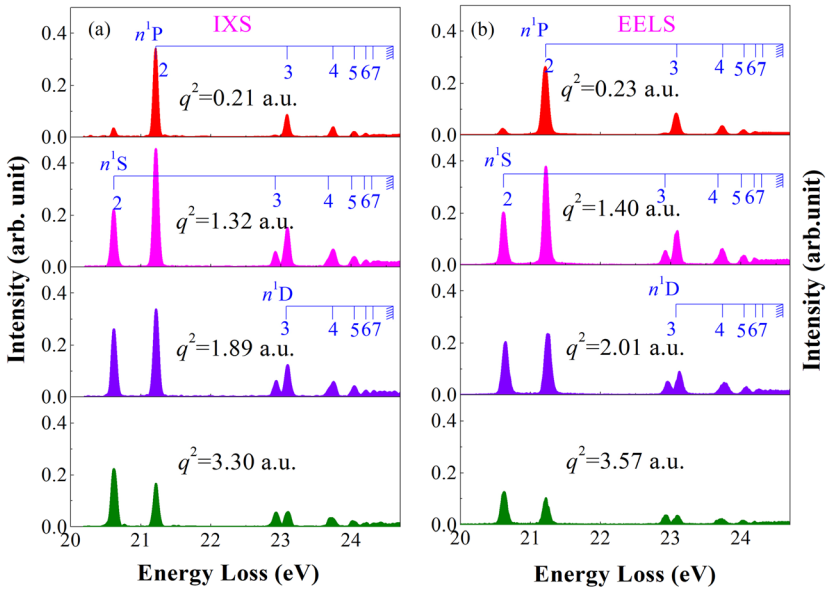

FIG. 4. (a) Experimental IXS spectra and (b) fast EELS spectra of helium gas as functions of energy loss at different squared momentum transfers with an energy resolution of about 70 meV. The peaks are labeled by the final states excited from the $1s^{21}S_0$ ground state. The IXS spectra were recorded at an incident photon energy of about 10 keV and the EELS spectra were collected at an impact electron energy of 2.5 keV. Reprinted with permission from Zhu *et al.*, J. Phys. B: At., Mol. Opt. Phys. **44**, 025203 (2011). Copyright 2011 IOP Publishing.

such as the pressures of the target are different. The similar characteristics observed in Fig. 4 provide clear evidence of the intrinsic equality of IXS and high-energy EELS for exploring the excitation mechanisms of atoms and molecules.

To provide a quantitative comparison, the ISFFs of the 2^1S_0 and 2^1P_1 states of helium measured by IXS and EELS are shown in Fig. 5. The excellent agreement of the IXS[8] and EELS[41] ISFFs at 1500 eV, as well as the theoretical ISFFs,[34,35] indicates the feasibility and reliability of the NRIXS method, which paves the way for electronic structure studies of the ground and excited states of atoms and molecules in the gas phase. It can also be seen that the apparent ISFFs measured by EELS at 200 eV and 400 eV[40] approach the IXS and theoretical ISFFs with increasing electron impact energies, which is evidence that that the FBA is satisfied by IXS. Consequently, the IXS data can serve as the high-energy limit of electron impact and can be used to test the conditions for the validity of the FBA in electron impact experiments. It should be pointed out that in general for complex systems such as multi-electron atoms and molecules, there is a lack of reliable theoretical calculations. Furthermore, determination of the conditions under which the FBA is valid in electron collisions is a trial-and-error procedure, i.e., there is no exact electron impact energy at which the FBA is approached for all atoms and molecules. For an atom or a molecule, the conditions under which the FBA is valid are different for different excitations. Even for the same transition, the FBA is valid in the small-q^2 region but is not valid in the large-q^2 region. Therefore, IXS studies are of crucial importance for investigations of the electronic structures of atoms and molecules.

Figure 6(a) presents the IXS and EELS GOSs of the dipole-allowed excitation of $b^1\Pi_u\,(\nu'=3)$ of N_2,[25,42] and it is clear that the two results are in excellent agreement, which indicates that the FBA is satisfied at an incident electron energy of 1500 eV. In 2001, Kim developed a semi-empirical theoretical method, namely, the BE-scaling method, based on the scaled plane-wave Born models, to obtain the ICSs of the dipole-allowed transitions of atoms and molecules.[43] The BE-scaling method has the advantage of producing

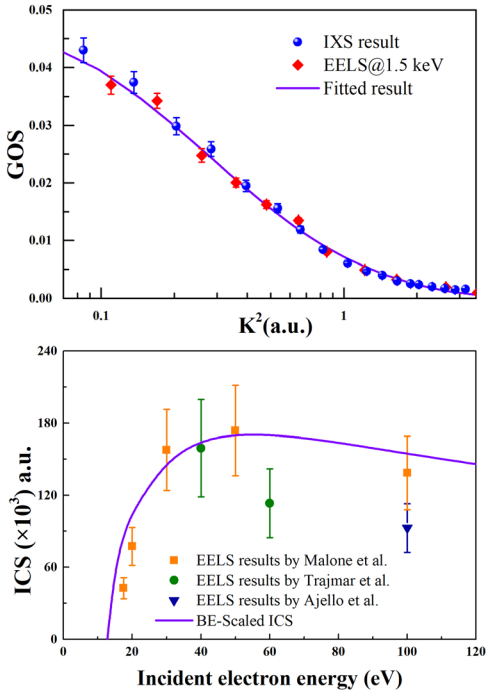

FIG. 6. (a) IXS and EELS GOSs of the dipole-allowed $b\,^1\Pi_u(\nu'=3)$ excitation of N_2. (b) BE-scaled ICSs of the $b\,^1\Pi_u(\nu'=3)$ state along with the EELS results.

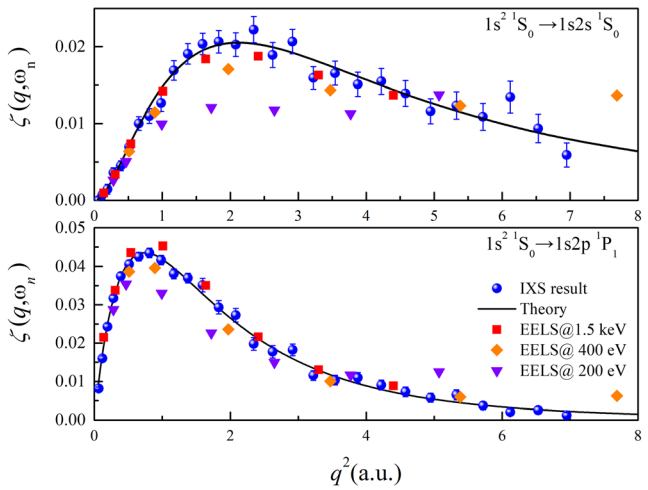

FIG. 5. IXS-derived ISFFs of the 2 ^1S and 2 ^1P states of helium along with EELS ISFFs determined at different impact electron energies (200 eV and 400 eV;[40] 1.5 keV[41]).

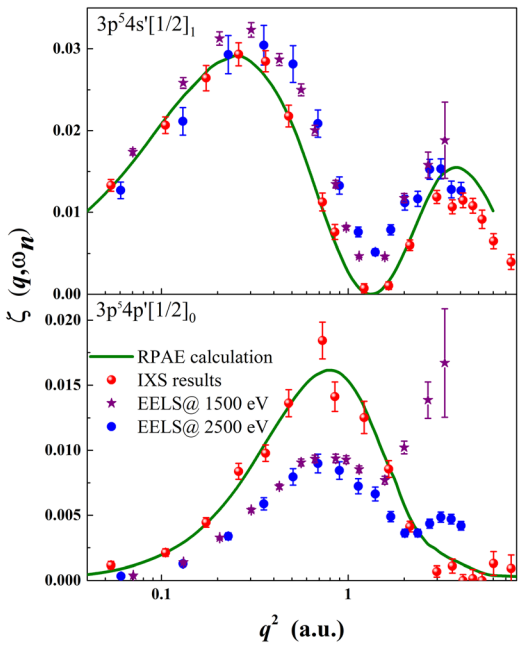

FIG. 7. IXS-derived ISFFs of the $3p^54s'[1/2]_1$ and $3p^54p'[1/2]_0$ states of argon along with EELS ISFFs determined at different impact electron energies (1500 eV;[48] 2500 eV[47]), as well as the theoretical results from the RPAE method.[49]

reliable ICSs at low impact electron energies and bridges the wide gap between low-energy and high-energy electron scattering. The BE-scaling method has been used to obtain reliable ICSs of the dipole-allowed valence-shell excitations of atoms and molecules. However, for application of the BE-scaling method, the availability of reliable GOSs is a prerequisite. For molecular nitrogen, the good match between the IXS and EELS GOSs shown in Fig. 6(a) excludes any systematic experimental errors, and the cross-checked experimental GOSs can serve as a benchmark. Therefore, the BE-scaled ICSs of $b^1\Pi_u$ ($v' = 3$) can be obtained from the present experimental GOSs. The BE-scaled ICSs of the $b^1\Pi_u$ ($v' = 3$) are presented in Fig. 6(b). The agreement with the low-energy electron impact results[44–46] obtained by integrating the DCSs from 0° to 180° is achieved, which further supports the applicability of the BE-scaling method. By utilizing the same method with other atoms and molecules, many ICSs data that have extensive applications in astrophysics and atmospheric physics have recently been reported by our group.[25–28]

Figures 7(a) and 7(b) present the ISFFs of the dipole-allowed transition of $3p^5 4s'[1/2]_1$ and the dipole-forbidden monopole-allowed transition of $3p^5 4p'[1/2]_0$ of argon measured by NRIXS and EELS.[33,47,48] It can be seen from Fig. 7(a) that for the dipole-allowed transition $3p^5 4s'[1/2]_1$, the EELS results are in good agreement with the IXS ones and the random phase approximation with exchange (RPAE)[49] calculations at $q^2 < 0.3$ a.u., which means that the FBA is approached for $E_0 > 1.5$ keV in this q^2 region. However, the EELS data are clearly larger than the IXS and RPAE ones near the minimum. This phenomenon is understandable since the minimum of the ISFF means that the contribution from the FBA is zero, and the observed intensity is due completely to the contribution from the higher Born series beyond the FBA. The ISFFs of the $3p^5 4s'[1/2]_1$ show the difficulty in reaching the FBA: i.e., impact electron energies of several keV, which is more than a hundred times higher than the transition energies, cannot guarantee the applicability of the FBA, even for not-so-large squared momentum transfers less than 2 a.u. However, it is clear from Fig. 7(a) that the IXS ISFFs satisfy the FBA and can serve as the high-energy limit of electron impact.

Figure 7(b) shows clearly that for the electric monopolar excitation of $3p^5 4p'[1/2]_0$, the IXS ISFFs match the calculations using the RPAE[49] very well, and provide the high-energy limit of the electron impact results. However, as can be seen in Fig. 7(b), the EELS apparent ISFFs measured at 1500 eV and 2500 eV are in agreement with each other at $q^2 < 1$ a.u. but are lower than the IXS and theoretical results. A similar phenomenon has been observed for the dipole-forbidden $a^1\Pi_g + w^1\Delta_u$ states of nitrogen, as shown in Fig. 8, where a wide range of incident electron energies from several hundreds of eV to tens of keV have been used. This phenomenon in which the coincident EELS results with different impact energies deviate from the FBA result is strange, since it has long been widely believed that a good match among fast-electron scattering results with higher and higher impact energies demonstrates the validity of the FBA. The dipole-allowed excitations of helium, nitrogen, and argon as well as the dipole-forbidden excitation of 2^1S_0 of helium satisfy this criterion, as mentioned above. However, the criterion is violated for the dipole-forbidden transitions of $3p^5 4p'[1/2]_0$ of Ar and $a^1\Pi_g + w^1\Delta_u$ of N_2. Therefore, the empirical criterion of a good match of the ISFFs or the GOSs measured at different electron energies for determining the validity of the FBA is not a strict one, and our understanding of electron scattering with multi-electron systems is far from complete.

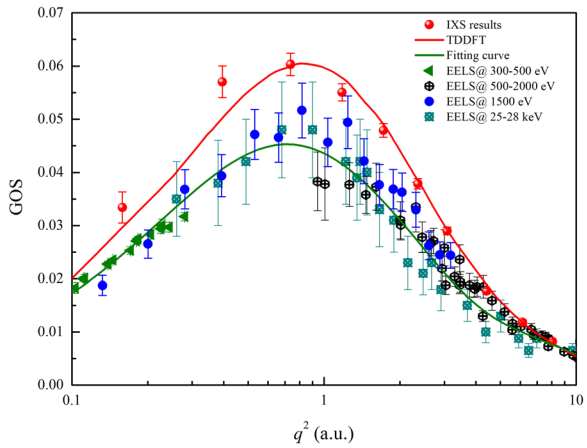

FIG. 8. IXS GOSs[20] along with EELS results at different impact electron energies (300 eV–500 eV;[50] 500 eV–2000 eV;[51] 25 keV–28 keV[52]). The red solid line is the calculated GOS with time-dependent density functional theory (TDDFT)[37] and the green solid line is the fitted curve of all the EELS data. Reprinted with permission from Kang *et al.*, J. Phys. B: At., Mol. Opt. Phys. **52**, 245202 (2019). Copyright 2019 IOP Publishing.

B. Compton profile

The first two Compton profile studies of gaseous He, Ar, Xe, and N_2 using a third-generation synchrotron radiation source were carried out on the BL08W beamline of SPring-8[53,54] in 2011. Subsequent Compton profile investigations of gaseous H_2 and some small alkane molecules were carried out by our group and collaborators.[22–24] As an example, Fig. 9 shows the Compton profile of molecular hydrogen, which was measured on the BL15U beamline of the SSRF, with an incident photon energy of about 20 keV and an energy spread of about 3 eV. It is clear from Fig. 9(a) that the raw X-ray scattering spectrum includes the Compton and elastic scattering peaks. The former is actually the real Compton profile convoluted with the experimental energy resolution, which gives a momentum spread. Therefore, the theoretical Compton profile should be convoluted with the experimental momentum resolution for comparison with the experimental measurement. Figure 9(b) shows the experimental Compton profile of H_2 along with the theoretical calculations using different packages as indicated in the key on the figure. In fact, the results from the different calculations coincide, and excellent agreement is achieved between them and the experimental results. However, a detailed comparison shows the importance of the electron correlation effect in describing the electronic structure of H_2.[22] It should be be mentioned that at present, solid state detectors are being used to detect the scattered photons, and their energy resolution of several hundreds of eV, which is much larger than the energy spread of the incident photons, is the main factor limiting the momentum resolution. This makes it difficult to obtain the detailed information about the ground state electronic structures of atoms and molecules. To overcome this shortcoming, a high impact photon energy and a larger scattering angle are preferred in experiments.

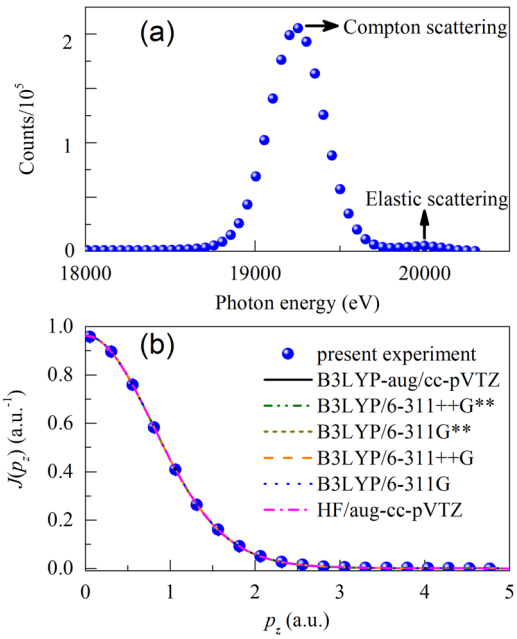

FIG. 9. (a) Compton scattering spectrum measured at 90° for H_2. (b) Compton profile of H_2. Reprinted with permission from Zhao *et al.*, Chin. Phys. B **24**, 033301 (2015). Copyright 2015 Chinese Physical Society.

C. Elastic squared form factor

Elastic scattering is the simplest X-ray scattering process, in which the incident photon energy does not change, i.e., the final state of the sample is the same as the initial state. By analyzing the scattering intensities as a function of momentum transfer, one can obtain the Fourier transform of the ground-state electron density distribution in position space. In contrast to the case of inelastic scattering, where fast electron scattering is equivalent to NRIXS under the FBA, in the case of elastic scattering, the contribution from the nuclei needs to be taken into account for electron scattering but not for X-ray scattering. For example, for elastic electron scattering by molecular hydrogen, the interaction can be represented in the potential term as

$$V = -\sum_{j=1}^{2}\frac{1}{|\boldsymbol{r}-\boldsymbol{r}_j|}+\frac{1}{|\boldsymbol{r}-\boldsymbol{R}_a|}+\frac{1}{|\boldsymbol{r}-\boldsymbol{R}_b|}, \tag{38}$$

where $\boldsymbol{R}_a$ and $\boldsymbol{R}_b$ are the position vectors of the nuclei, and $\boldsymbol{r}$ and $\boldsymbol{r}_j$ are the position operators of the incident electron and the bound electrons, respectively. The resulting DCS has two additional parts due to the interaction with the nucleus:

$$\begin{aligned}\left(\frac{d\sigma}{d\Omega}\right)_e &= \frac{4}{q^4}|\langle\Psi_0|\left[\exp(i\boldsymbol{q}\cdot\boldsymbol{R}_a)+\exp(i\boldsymbol{q}\cdot\boldsymbol{R}_b)\right.\\ &\quad\left.-\sum_{j=1}^{2}\exp(i\boldsymbol{q}\cdot\boldsymbol{r}_j)\right]|\Psi_0\rangle|^2\\ &= \frac{1}{\pi}\iint\sin\theta\,d\theta\,d\phi\left|\int\psi_0^{\nu*}\left[2\cos(\boldsymbol{q}\cdot\boldsymbol{R}/2)-\epsilon_0(\boldsymbol{q};\boldsymbol{R},\theta,\phi)\right]\psi_0^{\nu}\right|^2,\end{aligned} \tag{39}$$

where Ψ_0 and ψ_0^{ν} are the wave functions of the ground state and its vibrational part, and $\epsilon_0(\boldsymbol{q};\ \boldsymbol{R},\ \theta,\ \phi)$ and $\cos(\boldsymbol{q}\cdot\boldsymbol{R}/2)$ are the electron–electron and electron–nuclei scattering terms, respectively. It is clear from Eq. (39) that the interference effect prevents extraction of electronic structure information from the experimental elastic DCS by fast electron scattering, whereas it can be obtained from elastic X-ray scattering according to Eq. (19).

Elastic X-ray scattering measurements with H_2 were performed on the Taiwan Beamline BL12XU of SPring-8 with an incident photon energy of about 9989 eV and an energy resolution of about 70 meV. The deduced ESFFs are presented together with theoretical results in Fig. 10, from which it can be seen that there is good agreement between theory and experiment. The experimental results show that elastic X-ray scattering has a unique advantage over fast electron scattering in determining the pure electronic structure of the ground state of a molecule.

The situation for atoms is different, where the atomic matrix element from the nucleus is a constant Z, i.e., the atomic number. The reason is that the nucleus is located at the center of the atom, and so the pure electronic structure can be extracted from fast electron elastic scattering under the FBA. However, the different scattering mechanisms in elastic X-ray and electron scattering can provide deep insight into the scattering process. Recent comparative investigations of elastic X-ray and fast electron scattering from helium have elucidated an anomalous phenomenon first observed 40 years ago, namely, a large deviation of the elastic DCS from the FBA in the small-q^2 region. This can now be explained as being due to the dramatic enlargement of the contribution beyond the FBA in the small-q^2 region.[56] Furthermore, the ESFF of molecules measured by X-ray scattering has recently been used to extract bond lengths.[19]

D. Optical oscillator strength

The absolute OOS of an atom or a molecule is equivalent to the integral photoabsorption cross section, which represents the transition probability between the initial and final states and is essential for understanding photon emission and photon absorption processes.

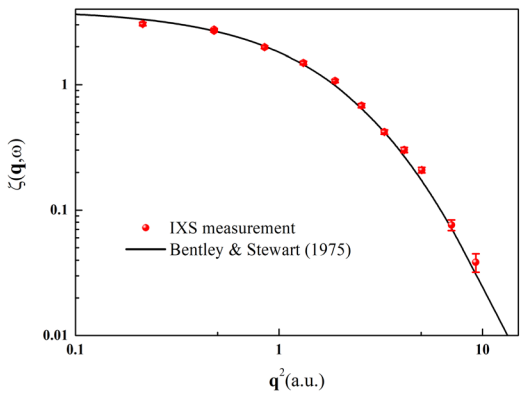

FIG. 10. Elastic squared form factor $\zeta(\boldsymbol{q})$ of molecular hydrogen. The solid red circles and the black solid line are the IXS measured data and the theoretical results obtained by Bentley and Stewart[55] using the Davidson–Jones (DJ) wave function. Reprinted with permission from Liu *et al.*, Phys. Rev. A **89**, 014502 (2014). Copyright 2014 American Physical Society.

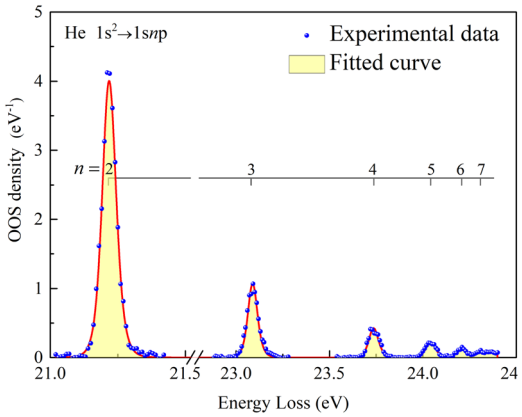

FIG. 11. IXS spectrum of helium with the valence-shell excitations assigned. Solid blue circles are the present experimental data and the shaded curve is the fitted result. The vertical axis has been converted into absolute OOS density.

Accurate OOS data for atoms and molecules are important in a variety of disciplines, including plasma science, astrophysics, and atmospheric physics, since photon emission and absorption processes are widespread in plasmas, interstellar space, and planetary atmospheres. The most commonly used methods to determine the OOS are the photoabsorption and dipole (e, e) methods, which suffer from line saturation and the rapid variation of the Bethe–Born conversion factor. The accuracy of the obtained OOSs might be influenced by these defects of the method. Therefore, we have proposed and realized the dipole (γ, γ) method, which can overcome the difficulties encountered by the photoabsorption and dipole (e, e) methods. OOSs cross-checked by different experimental methods constitute benchmark data for use across disciplines and provide a stringent test of state-of-the-art theoretical atomic and molecular codes.

Figure 11 presents a typical IXS spectrum of He with the valence-shell excitations assigned.[21] The solid blue circles are the experimental OOS densities and the red line is the fitted curve of the measured data. The peak areas are actually the OOSs of the corresponding transitions. The experimental OOS values are presented and compared with previously available experimental data as well as the results of theoretical calculations in Fig. 12. The excellent agreement with the literature data confirms the applicability of the dipole (γ, γ) method to the determination of OOS for gaseous samples.[21]

The OOSs of the valence-shell excitations for astrophysically relevant molecules, such as CO,[72] N_2,[73] Ar,[74] H_2,[75] and D_2[32] have been determined by our group using the dipole (γ, γ) method. The cross-checked OOS data can thus be used to model observed astrophysical spectra.

V. SUMMARY AND OUTLOOK

Essentially within the last decade, non-resonant X-ray scattering spectroscopy has been extended to explore the electronic structures and obtain the benchmark dynamic parameters of gaseous atoms and molecules. A new experimental method, dipole (γ, γ), has been proposed and realized to determine OOSs for the valence-shell excitations of atoms and molecules. The state-resolved ISFFs, ESFFs, OOSs, and ICSs, and the Compton profiles, of many atoms and molecules have been determined with high accuracy, and a unified absolutization criterion, namely, highly accurate and highly precise ISFFs and OOSs of the 2^1P state of helium, has been established. NRIXS has the remarkable advantages of exciting dipole-forbidden transitions at large momentum transfer and always satisfying the FBA. The former advantage can be used to study the electronic structures and excitation behaviors of dipole-forbidden transitions of atoms and molecules, and the latter allows the experimental results obtained to serve as the high-energy limit of electron impact and to be used to study the conditions under which the FBA is valid for electron collisions.

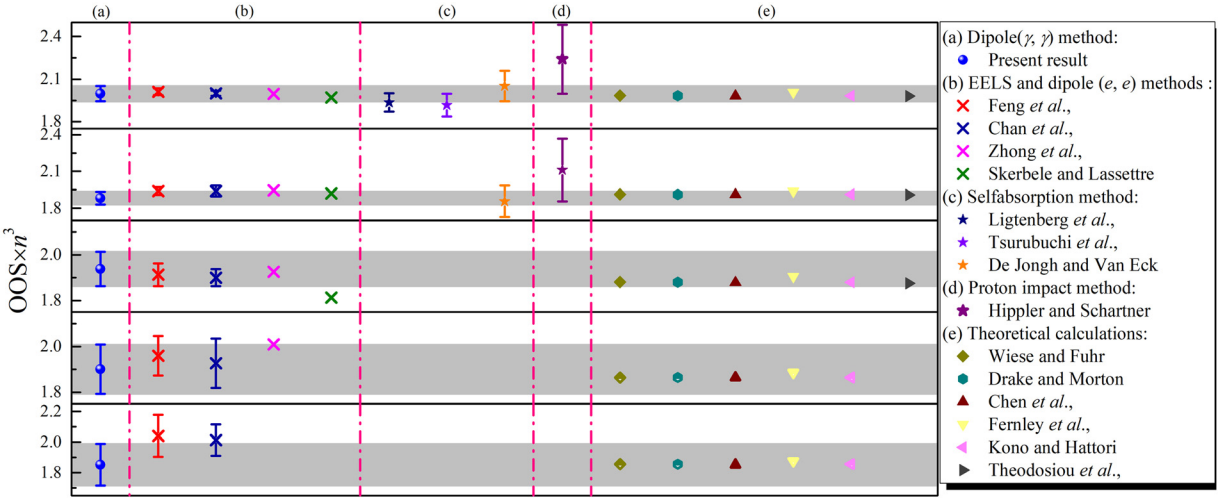

FIG. 12. OOSs of the $n\,^1P_1$ states of helium ($n = 3, \ldots, 7$, from top to bottom). (a) The blue circles are the present results with the dipole (γ, γ) method. (b) Experimental data from EELS or the dipole (e, e) method.[57–60] [(c) and (d)] Measured data from the self-absorption[61–63] and proton impact methods.[64] (e) Theoretically calculated data available in the literature.[65–71]

The intrinsic equivalence of NRIXS and fast EELS under the FBA makes cross-checking experimental results by different techniques feasible. Such cross checks can be used to exclude possible systematic experimental errors and to establish experimental benchmarks, as well as providing deep insight into the excitation process and revealing new collision and excitation mechanisms. The benchmark dynamic parameters for the ground and excited states of many atoms and molecules, including the ISFFs, ESFFs, OOSs, and Compton profiles, have been obtained. It has been found that an empirical criterion that has been widely accepted for electron impacts, namely, that a good match among fast electron scattering results with higher and higher incident electron energies is enough to demonstrate the validity of the FBA, may be problematic.[20] The different mechanisms of elastic scattering of X-rays and electrons explain the anomalous asymptotic behavior of elastic electron scattering from helium first observed more than 40 years ago.[56] Furthermore, vibronic and isotope effects have been observed.[76–78]

It is worth mentioning that every experimental technique has its own merits and demerits. One merit of EELS is the large scattering cross section, and one of its demerits is the strong interaction between incident electrons and the target, which leads to invalidity of the FBA and thus complicates the explanation of experimental observations. Furthermore, the DCS of high-energy electron scattering decreases rapidly at a rate of q^{-4} as the momentum transfer increases, so it is difficult to measure dynamic parameters at large momentum transfer. The IXS method, on the other hand, has the advantage that the FBA is almost always satisfied, and it is thus a powerful tool to study the dynamic parameters and electronic structures of the ground and excited states of atoms and molecules. IXS has the disadvantage of very low cross sections of about 10^{-25} cm^2, and this is why a high target pressure of about 1 Mpa is needed for IXS, compared with only about 0.01 Pa in electron scattering experiments. However, the DCS of IXS is determined only by the ISFFs and is independent of momentum transfer, and therefore IXS is suitable for measuring dynamic parameters at large momentum transfer. Combining different experimental techniques is helpful to gain accurate and complete information about atoms and molecules, and also gives deep insight into excitation mechanisms.

For OOS measurements, the newly developed dipole (γ, γ) method has the merit that it is free from the line saturation effect and its Bethe–Born conversion factor is nearly independent of excitation energy, and it is thus free from any systematic error and can achieve highly accurate results. However, it is limited by low cross sections and a moderate energy resolution of tens of meV. Although for strong transitions, the photoabsorption method is subject to the line saturation effect, it has the highest energy resolution when used to determine the oscillator strengths of rotational states. The dipole (e, e) method has large cross sections and is also not influenced by the line saturation effect, but its energy resolution is only sufficient to measure the OOSs of vibronic states at present. Furthermore, the rapid variation of the Bethe–Born conversion factor in the dipole (e, e) method may lead to some unknown uncertainties. It should be pointed out that the IXS technique is under continual development. When we began OOS measurements with the dipole (γ, γ) method in 2015, the energy resolution was just about 70 meV and the signal-to-noise ratio was rather poor owing to the low cross section and the very small scattering angle of the measurements.[72–74] However, since 2018, the energy resolution has been improved to 25 meV and the background signal has been reduced to about 1 count per 100 s, which improves the precision of the results.[32,75]

The main limitation of the X-ray scattering technique is still its very low cross sections, especially for the dilute gas targets used in atomic and molecular physics. However, IXS has a bright future owing to the rapid development of photon sources and of detection and analysis techniques. High-repetition-frequency hard X-ray FELs and fourth-generation synchrotron radiation sources are under construction in many countries, and these will boost the brilliance of X-ray beams by several orders of magnitude. The use of multi-analyzer and position-sensitive detectors[79,80] will increase the collection and detection efficiencies. All these technical developments will overcome the difficulties caused by the very low X-ray scattering cross sections.

Hard X-rays have strong penetrability, and the IXS is a "photon-in photon-out" technique, and therefore the sample environment is not a limitation. This provides an opportunity for studying the dynamic behaviors of free atoms and molecules under extreme conditions, for example at very high or low temperatures[81] or under very high pressures such as the several hundreds of megapascals in a diamond anvil cell. The electrically neutral nature of the photon makes it suitable for determining the dynamic parameters of atoms and molecules in strong electric and magnetic fields, which are very useful for fusion science and plasma physics, where strong electromagnetic environments are common.

At a low energy resolution of 1 eV, the incident photon flux can be increased by several orders of magnitude, and a wide energy loss region can be scanned. Thus, inner-shell excitations, which generally have large intervals, can be excited and resolved efficiently. However, very few investigations of such excitations have been carried out to date.[31,37,82] Recently, we have constructed a NRIXS spectrometer on the BL15U beamline at the SSRF with an energy resolution of 1.3 eV, which will be dedicated to studying the inner-shell excitations of atoms and molecules.[83]

ACKNOWLEDGMENTS

Many people have been involved in the work to extend NRIXS to atomic and molecular physics reviewed here, and they are too numerous for them all to be mentioned here. We are particularly grateful to our colleagues and the students who have graduated from our group: K. Yang, D. L. Feng, N. Hiraoka, K. D. Tsuei, X. Kang, D. D. Ni, T. Xiong, L. Q. Xu, X. L. Zhao, B. P. Xie, and Y. W. Liu. We acknowledge financial support from the National Natural Science Foundation of China (Grant Nos. U1932207 and U1732133) and the National Key Research and Development Program of China (Grant Nos. 2017YFA0303500 and 2017YFA0402300). The experiments reviewed here were supported by the beamtime approved by the Japan Synchrotron Radiation Research Institute, the National Synchrotron Radiation Research Center (NSRRC), and the Shanghai Synchrotron Radiation Facility (SSRF).

REFERENCES

[1] B. Crasemann and F. Wuilleumier, "Atomic physics with synchrotron radiation," Phys. Today **37**(6), 34 (1984).
[2] A. H. Compton, "The spectrum of scattered X-rays," Phys. Rev. **22**, 409 (1923).

[3]W. Schülke, *Electron Dynamics by Inelastic X-Ray Scattering* (Oxford University Press, 2007).
[4]J. W. M. Du Mond, "Compton modified line structure and its relation to the electron theory of solid bodies," Phys. Rev. **33**, 643 (1929).
[5]J. R. Schneider, "FLASH—from accelerator test facility to the first single-pass soft X-ray free-electron laser," J. Phys. B: At., Mol. Opt. Phys. **43**, 194001 (2010).
[6]P. Emma, R. Akre, J. Arthur *et al.*, "First lasing and operation of an ångstrom-wavelength free-electron laser," Nat. Photonics **4**, 641 (2010).
[7]D. Pile, "First light from SACLA," Nat. Photonics **5**, 456 (2011).
[8]B. P. Xie, L. F. Zhu, K. Yang, B. Zhou, N. Hiraoka, Y. Q. Cai, Y. Yao, C. Q. Wu, E. L. Wang, and D. L. Feng, "Inelastic X-ray scattering study of the state-resolved differential cross section of Compton excitations in helium atoms," Phys. Rev. A **82**, 032501 (2010).
[9]L. F. Zhu, L. S. Wang, B. P. Xie, K. Yang, N. Hiraoka, Y. Q. Cai, and D. L. Feng, "Inelastic X-ray scattering study on the single excitations of helium," J. Phys. B: At., Mol. Opt. Phys. **44**, 025203 (2011).
[10]H.-C. Tian, L.-Q. Xu, and L.-F. Zhu, "Selection rules for electric multipole transition of triatomic molecule in scattering experiments," Chin. Phys. B **27**, 043101 (2018).
[11]L. F. Zhu, W. Q. Xu, J. M. Sun, and W. Y. Zhang, "Optically forbidden transition of $A'^3\Delta_u \leftarrow X^3\Sigma_g^-$ in oxygen," Chin. Phys. Lett. **27**, 113301 (2010).
[12]H. Mark and K. Schocken, "Über die azimutale verteilung der an einem idealen gas gestreuten röntgenstrahlen," Naturwissenschaften **15**, 139–140 (1927).
[13]C. S. Barrett, "The scattering of X-rays from gases," Phys. Rev. **32**, 22 (1928).
[14]J. W. M. DuMond and H. A. Kirkpatrick, "A direct spectrum of the structure and shift of the Compton line with helium gas as the scatterer," Phys. Rev. **52**, 419 (1937).
[15]P. Eisenberger, "Electron momentum density of He and H_2; Compton X-ray scattering," Phys. Rev. A **2**, 1678 (1970).
[16]P. Eisenberger and W. A. Reed, "Gamma-ray Compton scattering: Experimental Compton profiles for He, N_2, Ar, and Kr," Phys. Rev. A **5**, 2085 (1972).
[17]D. D. Ni, X. Kang, K. Yang, Y. W. Liu, X. X. Mei, X. L. Zhao, L. Q. Xu, N. Hiraoka, K. D. Tsuei, and L. F. Zhu, "Squared form factors for the $A^1\Pi$ and $B^1\Sigma^+$ vibronic bands of carbon monoxide studied by high-resolution inelastic x-ray scattering," Phys. Rev. A **91**, 042501 (2015).
[18]Y. W. Liu, X. X. Mei, X. Kang, K. Yang, W. Q. Xu, Y. G. Peng, N. Hiraoka, K. D. Tsuei, P. F. Zhang, and L. F. Zhu, "Determination of the electronic structure of atoms and molecules in the ground state: Measurement of molecular hydrogen by high-resolution X-ray scattering," Phys. Rev. A **89**, 014502 (2014).
[19]X.-C. Huang, L.-Q. Xu, D.-D. Ni, Y.-W. Liu, Y.-G. Peng, K. Yang, N. Hiraoka, K.-D. Tsuei, and L.-F. Zhu, "Elastic squared form factor and binding effect of carbon dioxide studied by the high resolution X-ray scattering," J. Electron Spectrosc. Relat. Phenom. **226**, 41–44 (2018).
[20]X. Kang, L.-Q. Xu, Y.-W. Liu, S.-X. Wang, K. Yang, Y.-G. Peng, D.-D. Ni, N. Hiraoka, K.-D. Tsuei, and L.-F. Zhu, "A study on the validity of the first Born approximation for high-energy electron scattering with nitrogen molecules," J. Phys. B: At., Mol. Opt. Phys. **52**, 245202 (2019).
[21]L. Q. Xu, Y. W. Liu, X. Kang, D. D. Ni, K. Yang, N. Hiraoka, K. D. Tsuei, and L. F. Zhu, "The realization of the dipole (γ, γ) method and its application to determine the absolute optical oscillator strengths of helium," Sci. Rep. **5**, 18350 (2015).
[22]X.-L. Zhao, K. Yang, L.-Q. Xu, Y.-P. Ma, S. Yan, D.-D. Ni, X. Kang, Y.-W. Liu, and L.-F. Zhu, "Compton profile of molecular hydrogen," Chin. Phys. B **24**, 033301 (2015).
[23]X.-L. Zhao, K. Yang, L.-Q. Xu, X. Kang, Y.-W. Liu, Y.-P. Ma, S. Yan, D.-D. Ni, and L.-F. Zhu, "Investigation of Compton profiles of molecular methane and ethane," J. Chem. Phys. **142**, 084301 (2015).
[24]X.-X. Mei, X.-L. Zhao, L.-Q. Xu, Y.-W. Liu, X. Kang, S. Yan, D.-D. Ni, K. Yang, and L.-F. Zhu, "Investigation of Compton profile of molecular propane," Chin. Phys. Lett. **33**, 093301 (2016).
[25]Y. W. Liu, L. Q. Xu, D. D. Ni, X. Xu, X. C. Huang, and L. F. Zhu, "Integral cross sections of the dipole-allowed excitations of nitrogen molecule studied by the fast electron scattering," J. Geophys. Res. **122**, 3459–3468, https://doi.org/10.1002/2016ja023857 (2017).
[26]Y.-W. Liu, L.-Q. Xu, T. Xiong, X. Chen, K. Yang, N. Hiraoka, K.-D. Tsuei, and L.-F. Zhu, "Oscillator strengths and integral cross sections of the valence-shell excitations of the oxygen molecule studied by fast electron and inelastic X-ray scattering," Astrophys. J. Suppl. Ser. **238**, 26 (2018).
[27]Y.-W. Liu, L.-Q. Xu, T. Chen, D.-G. Qi, T. Xiong, and L.-F. Zhu, "Oscillator strengths and integral cross sections of the valence-shell excitations of acetylene studied by the high-energy electron-scattering," Astrophys. J. Suppl. Ser. **234**, 10 (2018).
[28]Y.-W. Liu, X.-J. Du, Y.-C. Xu, and L.-F. Zhu, "Oscillator strengths and integral cross sections of the valence-shell excitations of carbonyl sulfide studied by high-energy electron scattering," Astrophys. J. Suppl. Ser. **244**, 23 (2019).
[29]W. P. Healy, "A generalization of the Kramers-Heisenberg dispersion formula," Phys. Rev. A **16**, 1568 (1977).
[30]M. Blume, "Magnetic scattering of X rays (invited)," J. Appl. Phys. **57**, 3615–3618 (1985).
[31]J. A. Bradley, G. T. Seidler, G. Cooper, M. Vos, A. P. Hitchcock, A. P. Sorini, C. Schlimmer, and K. P. Nagle, "Comparative study of the valence electronic excitations of N_2 by inelastic X-ray and electron scattering," Phys. Rev. Lett. **105**, 053202 (2010).
[32]T. Xiong, Y. W. Liu, K. Yang, X. C. Huang, S. X. Wang, S. Yan, K. L. Yu, N. Hiraoka, K. D. Tsuei, and L. F. Zhu, "Optical oscillator strengths of the vibronic excitations of molecular deuterium determined by the dipole (γ, γ) method," Phys. Rev. A **98**, 042509 (2018).
[33]X. Kang, K. Yang, Y. W. Liu, W. Q. Xu, N. Hiraoka, K. D. Tsuei, P. F. Zhang, and L. F. Zhu, "Squared form factors of valence-shell excitations of atomic argon studied by high-resolution inelastic X-ray scattering," Phys. Rev. A **86**, 022509 (2012).
[34]N. M. Cann and A. J. Thakkar, "First Born differential cross-sections for electronic excitation in the helium atom," J. Electron Spectrosc. Relat. Phenom. **123**, 143–159 (2002).
[35]X. Y. Han and J. M. Li, "High-energy electron-impact excitation process: The generalized oscillator strengths of helium," Phys. Rev. A **74**, 062711 (2006).
[36]M. Inokuti, "Inelastic collisions of fast charged particles with atoms and molecules-the Bethe theory revisited," Rev. Mod. Phys. **43**, 297 (1971).
[37]J. A. Bradley, A. Sakko, G. T. Seidler, A. Rubio, M. Hakala, K. Hämäläinen, G. Cooper, A. P. Hitchcock, K. Schlimmer, and K. P. Nagle, "Reexamining the Lyman-Birge-Hopfield band of N_2," Phys. Rev. A **84**, 022510 (2011).
[38]P. E. Grabowski and D. F. Chernoff, "Pseudospectral calculation of helium wave functions, expectation values, and oscillator strength," Phys. Rev. A **84**, 042505 (2011).
[39]X.-J. Liu, L.-F. Zhu, Z.-S. Yuan, W.-B. Li, H.-D. Cheng, J.-M. Sun, and K.-Z. Xu, "The generalized oscillator strengths for the valence shell excitations in helium by fast electron impact," J. Electron Spectrosc. Relat. Phenom. **135**, 15–20 (2004).
[40]M. A. Dillon and E. N. Lassettre, "A collision cross section study of the $1\,^1S\,2\,^1P$ and $1\,^1S\,2\,^1S$ transitions in helium at kinetic energies from 200-700 eV. Failure of the born approximation at large momentum changes," J. Chem. Phys. **62**, 2373–2390 (1975).
[41]K. Z. Xu, R. F. Feng, S. L. Wu, Q. Ji, X. J. Zhang, Z. P. Zhong, and Y. Zheng, "Absolute generalized oscillator strengths of $2\,^1S$ and $2\,^1P$ excitations of helium measured by angle-resolved electron-energy-loss spectroscopy," Phys. Rev. A **53**, 3081 (1996).
[42]Y. G. Peng, X. Kang, K. Yang, X. L. Zhao, Y. W. Liu, X. X. Mei, W. Q. Xu, N. Hiraoka, K. D. Tsuei, and L. F. Zhu, "Squared form factors of vibronic excitations in 12–13.3 eV of nitrogen studied by high-resolution inelastic X-ray scattering," Phys. Rev. A **89**, 032512 (2014).
[43]Y. K. Kim, "Scaling of plane-wave Born cross sections for electron-impact excitation of neutral atoms," Phys. Rev. A **64**, 032713 (2001).
[44]C. P. Malone, P. V. Johnson, X. Liu, B. Ajdari, I. Kanik, and M. A. Khakoo, "Integral cross sections for the electron-impact excitation of the $b\,^1\Pi_u$, $c_3\,^1\Pi_u$, $o_3\,^1\Pi_u$, $b'\,^1\Sigma_u^+$, $c_4'\,^1\Sigma_u^+$, $G^3\Pi_u$, and $F\,^1\Pi_u$ states of N_2," Phys. Rev. A **85**, 062704 (2012).
[45]S. Trajmar, D. F. Register, and A. Chutjian, "Electron scattering by molecules II. Experimental methods and data," Phys. Rep. **97**, 219–356 (1983).
[46]J. M. Ajello, M. H. Stevens, I. Stewart, K. Larsen, L. Esposito, J. Colwell, W. McClintock, G. Holsclaw, J. Gustin, and W. Pryor, "Titan airglow spectra from Cassini ultraviolet imaging spectrograph (UVIS): EUV analysis," Geophys. Res. Lett. **34**, L24204, https://doi.org/10.1029/2007GL031555 (2007).

[47]L. F. Zhu, H. D. Cheng, Z. S. Yuan, X. J. Liu, J. M. Sun, and K. Z. Xu, "Generalized oscillator strengths for the valence-shell excitations of argon," Phys. Rev. A **73**, 042703 (2006).
[48]T. Chen, Y.-W. Liu, Y.-C. Xu, and L.-F. Zhu, "Generalized oscillator strengths of the valence-shell excitations of argon studied by fast electron impact," J. Phys. B: At., Mol. Opt. Phys. **53**, 085201 (2020).
[49]Z. Chen, A. Z. Msezane, and M. Y. Amusia, "Generalized oscillator strength for the argon $3p^6$-$3p^5 4s$ transition: Correlation and exchange effects on the characteristic minimum," Phys. Rev. A **60**, 5115 (1999).
[50]A. Skerbele and E. N. Lassettre, "Absolute electron collision cross sections for two forbidden transitions in nitrogen at kinetic energies of 300–500 eV," J. Chem. Phys. **53**, 3806–3813 (1970).
[51]N. Oda and T. Osawa, "Generalised oscillator strength and total cross sections for the $X^1\Sigma_g^+$ $a^1\Pi_g$ transition in molecular nitrogen at 500 to 2000 eV incident electron energies," J. Phys. B: At., Mol. Opt. Phys. **14**, L563 (1981).
[52]R. S. Barbieri and R. A. Bonham, "Momentum-transfer dependence of the Lyman-Birge-Hopfield and the K-shell preionization lines in the nitrogen molecule by means of high-energy electron-impact spectroscopy," Phys. Rev. A **45**, 7929 (1992).
[53]H. Sakurai, H. Ota, N. Tsuji, M. Itou, and Y. Sakurai, "Accurate Compton scattering measurements of noble gases: The importance of electron correlations in heavy atoms," J. Phys. B: At., Mol. Opt. Phys. **44**, 065001 (2011).
[54]K. Kobayashi, M. Itou, T. Hosoya, N. Tsuji, Y. Sakurai, and H. Sakurai, "Accurate Compton scattering measurements for N_2 molecules," J. Phys. B: At., Mol. Opt. Phys. **44**, 115102 (2011).
[55]J. J. Bentley and R. F. Stewart, "Total X-ray scattering by H_2," J. Chem. Phys. **62**, 875–878 (1975).
[56]Y.-W. Liu, T. Xiong, X.-C. Huang, K. Yang, K.-L. Yu, N. Hiraoka, K.-D. Tsuei, and L.-F. Zhu, "An investigation of the anomalous asymptotic behavior of elastic electron scattering of helium," J. Chem. Phys. **152**, 034304 (2020).
[57]R. F. Feng, B. X. Yang, S. L. Wu, S. L. Xing, F. Zhang, Z. P. Zhong, X. Z. Guo, and K. Z. Xu, "High-resolution dipole (e, e) study for optical oscillator strengths of helium," Sci. China Ser. A: Math. **39**, 1288–1295 (1996).
[58]W. F. Chan, G. Cooper, and C. E. Brion, "Absolute optical oscillator strengths for the electronic excitation of atoms at high resolution: Experimental methods and measurements for helium," Phys. Rev. A **44**, 186 (1991).
[59]Z. P. Zhong, R. F. Feng, S. L. Wu, L. F. Zhu, X. J. Zhang, and K. Z. Xu, "Electron-impact study for the and (n = 3-6) excitations in helium," J. Phys. B: At., Mol. Opt. Phys. **30**, 5305 (1997).
[60]A. M. Skerbele and E. N. Lassettre, "Higher-resolution study of the electron-impact spectrum of helium," J. Chem. Phys. **40**, 1271–1275 (1964).
[61]R. C. G. Ligtenberg, P. J. M. van der Burgt, S. P. Renwick, W. B. Westerveld, and J. S. Risley, "Optical oscillator strengths of noble-gas resonance transitions in the vacuum-ultraviolet region," Phys. Rev. A **49**, 2363 (1994).
[62]S. Tsurubuchi, K. Watanabe, and T. Arikawa, "Optical oscillator strengths of the resonance lines of rare gases," J. Phys. Soc. Jpn. **59**, 497–505 (1990).
[63]J. P. De Jongh and J. Van Eck, "Oscillator strengths of the resonance lines of some rare gases," Physica **51**, 104–112 (1971).
[64]R. Hippler and K.-H. Schartner, "Absolute cross sections for the excitation of n ^1P-levels of helium by proton impact (150-1000 keV)," J. Phys. B: At., Mol. Opt. Phys. **7**, 618 (1974).
[65]W. L. Wiese and J. R. Fuhr, "Accurate atomic transition probabilities for hydrogen, helium, and lithium," J. Phys. Chem. Ref. Data **38**, 565–720 (2009).
[66]G. W. F. Drake and D. C. Morton, "A multiplet table for neutral helium (^{4}He I) with transition rates," Astrophys. J. Suppl. Ser. **170**, 251 (2007).
[67]M.-K. Chen, "Accurate oscillator strengths for S-P transitions in the He atom," J. Phys. B: At., Mol. Opt. Phys. **27**, 865 (1994).
[68]M.-K. Chen, "F values for high-lying s-p and p-d transitions in the He atom by selected B-spline basis functions," J. Phys. B: At., Mol. Opt. Phys. **27**, 4847 (1994).
[69]J. A. Fernley, K. T. Taylor, and M. J. Seaton, "Atomic data for opacity calculations. VII. Energy levels, f values and photoionisation cross sections for He-like ions," J. Phys. B: At., Mol. Opt. Phys. **20**, 6457 (1987).
[70]A. Kono and S. Hattori, "Accurate oscillator strengths for neutral helium," Phys. Rev. A **29**, 2981 (1984).
[71]C. E. Theodosiou, "Lifetimes of singly excited states in He I," Phys. Rev. A **30**, 2910 (1984).
[72]X. Kang, Y. W. Liu, L. Q. Xu, D. D. Ni, K. Yang, N. Hiraoka, K. D. Tsuei, and L. F. Zhu, "Oscillator strength measurement for the A(0–6)–X(0), C(0)–X(0), and E(0)–X(0) transitions of CO by the dipole (γ, γ) method," Astrophys. J. **807**, 96 (2015).
[73]Y.-W. Liu, X. Kang, L.-Q. Xu, D.-D. Ni, K. Yang, N. Hiraoka, K.-D. Tsuei, and L.-F. Zhu, "Oscillator strengths of vibrionic excitations of nitrogen determined by the dipole (γ, γ) method," Astrophys. J. **819**, 142 (2016).
[74]X. Xu, D.-D. Ni, X. Kang, Y.-W. Liu, L.-Q. Xu, K. Yang, N. Hiraoka, K.-D. Tsuei, and L.-F. Zhu, "The absolute optical oscillator strengths of the $3p^5 4s$ and excitations of argon measured by the dipole (γ, γ) method," J. Phys. B: At., Mol. Opt. Phys. **49**, 064010 (2016).
[75]T. Xiong, Y.-C. Xu, K. Yang, N. Hiraoka, and L.-F. Zhu, "Oscillator strengths for the Lyman and Werner bands of molecular hydrogen studied by the dipole (γ, γ) method," Astrophys. J. **885**, 163 (2019).
[76]D. D. Ni, L. Q. Xu, Y. W. Liu, K. Yang, N. Hiraoka, K. D. Tsuei, and L. F. Zhu, "Comparative study of the low-lying valence electronic states of carbon dioxide by high-resolution inelastic X-ray and electron scattering," Phys. Rev. A **96**, 012518 (2017).
[77]L. Q. Xu, X. Kang, Y. G. Peng, X. Xu, Y. W. Liu, Y. Wu, K. Yang, N. Hiraoka, K. D. Tsuei, J. G. Wang *et al.*, "Comparative study of inelastic squared form factors of the vibronic states of B $^1\Sigma_u^+$, C $^1\Pi_u$, and EF $^1\Sigma_g^+$ for molecular hydrogen: Inelastic X-ray and electron scattering," Phys. Rev. A **97**, 032503 (2018).
[78]L. Q. Xu, Y. G. Peng, T. Xiong, X. Xu, Y. W. Liu, Y. Wu, J. G. Wang, and L. F. Zhu, "Inelastic squared form factors of the vibronic states of B $^1\Sigma_u^+$, C $^1\Pi_u$, and EF $^1\Sigma_g^+$ for molecular hydrogen deuteride studied by fast electron scattering," Phys. Rev. A **98**, 012502 (2018).
[79]S. Huotari, C. J. Sahle, C. Henriquet, A. Al-Zein, K. Martel, L. Simonelli, R. Verbeni, H. Gonzalez, M.-C. Lagier, C. Ponchut *et al.*, "A large-solid-angle X-ray Raman scattering spectrometer at ID20 of the European Synchrotron Radiation Facility," J. Synchrotron Rad. **24**, 521–530 (2017).
[80]J. M. Ablett, D. Prieur, D. Céolin, B. Lassalle-Kaiser, B. Lebert, M. Sauvage, T. Moreno, S. Bac, V. Balédent, A. Ovono *et al.*, "The GALAXIES inelastic hard X-ray scattering end-station at Synchrotron SOLEIL," J. Synchrotron Rad. **26**, 263–271 (2019).
[81]J. Inkinen, J. Niskanen, A. Sakko, K. O. Ruotsalainen, T. Pylkkänen, S. Galambosi, M. Hakala, G. Monaco, K. Hämäläinen, and S. Huotari, "Interplay between temperature-activated vibrations and nondipolar effects in the valence excitations of the CO_2 molecule," J. Phys. Chem. A **118**, 3288–3294 (2014).
[82]J. Inkinen, A. Sakko, K. O. Ruotsalainen, T. Pylkkänen, J. Niskanen, S. Galambosi, M. Hakala, G. Monaco, S. Huotari, and K. Hämäläinen, "Temperature dependence of CO_2 and N_2 core-electron excitation spectra at high pressure," Phys. Chem. Chem. Phys. **15**, 9231–9238 (2013).
[83]D.-D. Ni, X. Kang, S. Yan, X.-C. Huang, T. Xiong, D.-X. Liang, K. Yang, and L.-F. Zhu, "A 1-m non-resonant inelastic X-ray scattering spectrometer at BL15U, Shanghai Synchrotron Radiation Facility," Rev. Sci. Instrum. **89**, 085108 (2018).